Proceedings of the ASME 2021
International Mechanical Engineering Congress and Exposition
IMECE2021
November 1-5, 2021, Virtual, Online

IMECE2021-73554

IN-SITU SCANNING ELECTRON MICROSCOPE CHEMICAL VAPOR DEPOSITION AS A PLATFORM FOR NANOMANUFACTURING INSIGHTS

Gordon Koerner[1], Ramakrishna Surya[1], Kannappan Palaniappan[2], Prasad Calyam[2], Filiz Bunyak[2], Matthew R. Maschmann[1]

[1]University of Missouri, Department of Mechanical & Aerospace Engineering, Columbia, MO, USA
[2]University of Missouri, Department of Electrical Engineering & Computer Science Engineering, Columbia, MO, USA

ABSTRACT

While the physical properties of carbon nanotubes (CNTs) are often superior to conventional engineering materials, their widespread adoption into many applications is limited by scaling the properties of individual CNTs to macroscale CNT assemblies known as CNT forests. The self-assembly mechanics of CNT forests that determine their morphology and ensemble properties remain poorly understood. Few experimental techniques exist to characterize and observe the growth and self-assembly processes in situ. Here we introduce the use of in-situ scanning electron microscope (SEM) synthesis based on chemical vapor deposition (CVD) processing. In this preliminary report, we share best practices for in-situ SEM CVD processing and initial CNT forest synthesis results. Image analysis techniques are developed to identify and track the movement of catalyst nanoparticles during synthesis conditions. Finally, a perspective is provided in which in-situ SEM observations represent one component of a larger system in which numerical simulation, machine learning, and digital control of experiments reduces the role of humans and human error in the exploration of CNT forest process-structure-property relationships.

Keywords: carbon nanotubes, in-situ, synthesis, scanning electron microscope

NOMENCLATURE

CNT	carbon nanotube
CVD	chemical vapor deposition
ESEM	environmental scanning electron microscope
HOF	Herman orientation factor
MEMS	micro-electrical mechanical system
RL	reinforcement learning
SAXS	small angle X-ray scattering
SEM	scanning electron microscope
TEM	transmission electron microscope

1. INTRODUCTION

Carbon nanotubes (CNTs) exhibit an array of exceptional engineering properties that frequently exceed conventional materials. Their unique blend of mechanical, thermal, and electrical properties may be advantageous in applications including multi-functional structural materials [1,2], flexible sensors [3,4], electronics [5,6], and thermal interface materials [7,8]. When produced in large populations, CNTs form vertically aligned films known as CNT forests (also known as CNT arrays, turfs, or carpets) that may grow to heights of several millimeters. The ensemble properties of CNT forests are typically degraded by orders of magnitude relative to those observed for individual CNTs. For example, the elastic modulus of an individual CNT may exceed 1 TPa, the modulus of CNT forests is on the order of 1-100 MPa [4,9–17]. The degradation of properties is typically attributed to CNT forest morphological features such as CNT waviness, kinks, and inhomogeneities in areal density. The specific mechanisms that govern these characteristics during the synthesis and self-assembly of CNT forests, however, remain poorly understood.

CNT forests are typically synthesized using chemical vapor deposition (CVD) methods. To begin the synthesis, a thin film transition metal catalyst film (typically iron or nickel) is deposited on a substrate. Often, an oxide buffer layer (typically alumina) is deposited between the substrate and the active catalyst film [18,19]. The substrate is then heated to 600-900°C to facilitate the CVD process. Heating is supplied by either an external furnace (hot-walled CVD), or the substrate provides the heating mechanism via resistive heating (cold-walled CVD). An inert carrier gas such as Ar or He delivers H_2 and a hydrocarbon gas (typically C_2H_2 or C_2H_4). Here, H_2 serves as a chemical reducing agent and the hydrocarbon gas is the feedstock to support CNT synthesis. At high temperature and in a reducing environment, the catalyst layer forms discrete catalyst nanoparticles that support the growth of CNTs.

The synthesis of CNTs and small CNT populations has been directly observed using in-situ transmission electron microscope (TEM) synthesis techniques [20–24]. In these techniques, CNT synthesis occurs within the chamber using cold-walled CVD techniques, with heating supplied by a thin film heating element embedded within a silicon microchip. Gas is provided to the chip either using direct vapor delivery within the TEM chamber (environmental TEM), or the gas is enclosed within a sealed membrane [25]. Dynamic image sequences are assisted by image acquisition rates that typically exceed 1,000 frames per second. The imaging resolution of TEM enables the direct imaging of individual CNTs during growth rather than population-averaged measurements. Using in-situ TEM techniques, researchers may examine the catalyst nanoparticles with atomic precision to identify relevant parameters that facilitate catalytic activity. More recently, the nucleation, self-assembly, and early growth of CNT forests were studied using in-situ TEM [23]. These studies were the first to directly observe the mechanical competition between contacting CNTs lengthening at different rates. The reaction forces generated were sufficient to kink multiwalled CNTs. While these studies represent an exciting advance, the limited depth of field and field width restrict the scope of observation. Further, because image acquisition in TEM is via transmission through a sample, the resulting image represents a projection through the height of a CNT forest, making height-resolved characterization difficult.

Small angle X-ray scattering (SAXS) measurements have also been used to characterize the morphology of CNT forests in situ during their synthesis and self-assembly [26–28]. The SAXS measurements provide interpretable data describing the CNT forest diameter distribution, CNT alignment along the growth axis, and CNT areal density. The data sets collected represent the population average results obtained within the diameter of the X-ray beam (40 μm) and the depth of the forest. The X-ray beam sampled the cross section of a growing CNT forest, providing height-resolved data. Typical data reveal that CNT forest areal density decreases when sampling from the top of the CNT forest downward towards the substrate [29,30]. The population-averaged CNT alignment along the growth axis, as quantified using the Herman Orientation Factor (HOF), becomes greatest several hundreds of microns below the top surface of the forest and is reduced closer to the growth substrate. The HOF at the top-most surface of the CNT forest is greatly diminished, representing the disorganized “crust” layer frequently observed at the free surface of CNT forests. The CNT diameter distribution is well represented by a log-normal distribution. The distribution mean is skewed to greater values moving away from the top surface of CNT forests, as smaller-diameter CNTs become more sparse [27]. Presumably, these CNTs are delaminated from the CNT growth substrate during the growth process.

Raman spectroscopy has also been used to characterize the synthesis of single-walled CNTs in-situ [31,32]. In this configuration, the Raman spectrometer laser provides heating to the top surface of isolated silicon oxide micropillars. Gas flow is provided within a cold-walled reactor. The synthesis conditions are chosen is such that isolated single-walled CNT synthesis is promoted [33]. Time-resolved Raman spectra provide an assessment of CNT quality and CNT growth rate.

After CNT forest synthesis, SEM characterization is among the most common characterization methods. The technique has sufficient resolution to distinguish individual multiwalled CNTs and catalyst nanoparticles while offering sufficient field width to capture up to millimeters of CNT length. The relatively large depth of field allows a user to view the morphology of CNTs that exist on the exposed surface and several microns into the surface. To date, however, reports of in-situ SEM syntheses of CNTs have been sparse [34], resulting in disorganized CNT bundles rather than dense CNT forests. The initial efforts to use in-situ SEM synthesis of CNT forests, including best practices and a forward-looking perspective of the technology are described here.

2. MATERIALS AND METHODS

A Protochips Fusion 350 stage and FEI Quanta 600F environmental scanning electron microscope (ESEM) was used for all experiments (see **FIGURE 1**). The stage was secured to the SEM stage using a set screw. Each experiment was conducting using a MEMS-based heating chip known as an E-chip. E-chips featuring a SiC thin film heating element that enables uniform heating of an area up to 300 x 300 μm were used. A schematic of a heating chip is shown in **FIGURE 2**, with an inset showing the infrared signature of the heated zone. The heating area contains a 3 x 3 array of holes. The chip configurations used in the current studies included (i) the bare SiC heating element and a (ii) the SiC heating element overlaid with a thin SiN layer. Electrical contact was established between the heating chip and the stage using spring-loaded contact arms. The heating rate and setpoint temperature were controlled using the Protochips Clarity control software using an external computer. Time sequences of SEM images are obtained using the SEM control software.

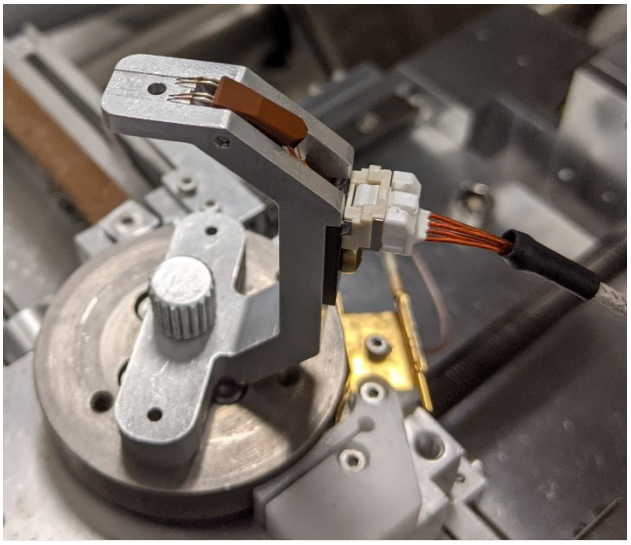

FIGURE 1. PROTOCHIPS SEM STAGE WITH ATTACHED FOUR CHANNEL CABLE INSTALLED WITHIN A FEI QUANTA ENVIRONMENTAL SEM CHAMBER.

Thin film catalyst layers were deposited on the E-chips by sputtering at a base pressure of 1 x 10^{-7} Torr. A SouthBay Technology ion beam sputtering system was used to deposit 10 nm of alumina and 2 nm of iron. A crystalline sapphire target was used as an alumina target, while a 99.99% pure iron target was used as a source of iron. The alumina layer acts as a diffusion barrier layer [18], while the iron layer acts as the active catalyst. Before deposition, the iron target was cleaned with the ion beam to remove possible surface oxidation and contamination. The catalyst thickness was monitored using a quartz crystal microbalance.

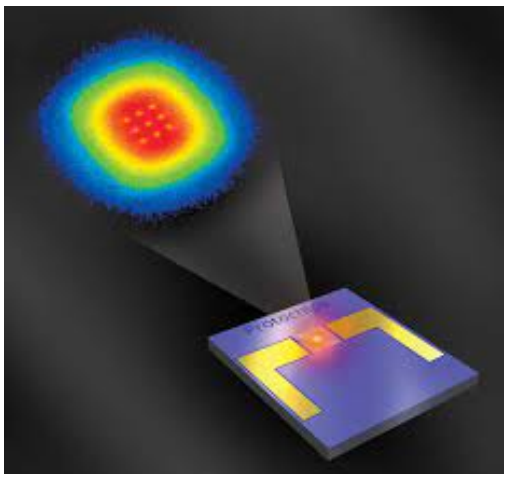

FIGURE 2. SCHEMATIC OF A PROTOCHIPS FUSION THERMAL E-CHIP. THE INSET SHOWS A MAGNIFIED REPRESENTATION OF THE HEATED REGION. FROM [35].

Acetylene was the only gas introduced to the SEM chamber. Conventional CNT forest synthesis experiments performed at atmospheric pressure typically include an inert carrier gas (Ar, He) and hydrogen in addition to a hydrocarbon gas such as acetylene. While hydrogen at atmospheric pressure chemically reduces the oxidized iron catalyst layer, recent in-situ TEM experiments have shown that hydrogen is ineffective at reducing oxidized iron at the pressures typical of electron microscopes [21]. The acetylene gas was first passed through a desiccant gas drier to remove residual water vapor. A cold trap was attached to the SEM chamber to condense water vapor contaminants and reduce the base pressure of the SEM. Liquid nitrogen or dry ice was used as a refrigerant. Stainless steel tubing was used to route acetylene from the gas cylinder to the SEM chamber. A pressure limiting aperture was used to enhance image resolution in the gaseous environment.

Surface treatment of the E-chips to reduce the surface energy of the heating chips and reduce the migration of iron nanoparticles during high-temperature processing. Plasma passivation was performed using a PELCO easiGlow glow discharge cleaning system. Treatment of the chips was performed at a base pressure of 0.2 Torr for a duration of 300 seconds.

After installing the SEM stage and chip, the system was pumped in high vacuum mode for a duration between 15 minutes to 16 hours (overnight). The SEM chamber was then flushed five times with acetylene gas by purging acetylene gas at a maximum pressure of 150 Pa. During experiments, the acetylene pressure was maintained by the FEI SEM software interface. Prior to experimentation, a cold trap affixed to the SEM was filled with liquid nitrogen to condense water vapor and other condensable vapors within the chamber that could interfere with the CNT synthesis. The base vacuum level in the chamber reached between 3 x 10^{-4} – 9 x 10^{-4} Pa (2.25 x 10^{-6} – 6.75 x 10^{-6} Torr) before introducing process gases. The typical imaging parameters include an acceleration voltage of 5 kV and a spot size (related to beam current) of 3.5. The typical working distance was 8 mm. Tuning of the image focus and stigmation was first performed in high vacuum.

Acetylene gas was introduced to the SEM chamber at a pressure between 10 – 50 Pa. The pressure was allowed to stabilize before the electron beam was turned on, and imaging conditions were readjusted to better match the requirements of the gaseous environment. The heating chips were heated at a rate of 5ºC/sec using closed-loop temperature control. Thermal drift of the chip was evident, but active image compensation was not attempted during the heating stage. Once the final synthesis temperature was reached, the imaging conditions were readjusted, if necessary. Stage translation and image magnification could be changed on the fly during the process.

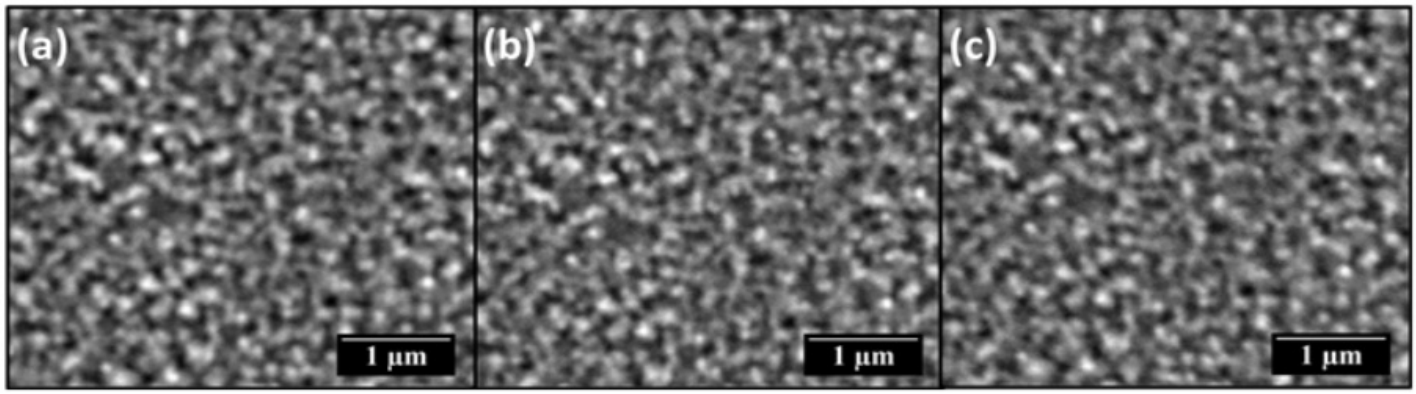

FIGURE 3: ABSENCE OF CATALYST REDUCTION (A) IMMEDIATELY AFTER THE SETPOINT TEMPERATURE WAS REACHED, (B) 30 MINUTES AFTER SETPOINT, AND (C) 1 HOUR AFTER SETPOINT TEMPERATURE WAS REACHED. THERE IS NO CHANGE IN PARTICLE BEHAVIOR, SUGGESTING HYDROGEN ALONE DID NOT REDUCE THE IRON CATALYST.

3. RESULTS AND DISCUSSION

3.1 Catalyst Evolution Studies

The first phase of CNT forest synthesis process is the chemical reduction of the iron catalyst film at or near the synthesis temperature, followed by the de-wetting of the film to form discrete nanoparticles. In an atmospheric pressure CVD synthesis, the reduction and catalyst particle evolution typically occurs within a diluted hydrogen environment. However, at the relatively low operating pressures of electron microscopes, hydrogen is ineffective at reducing the catalyst film within the typical timeframe of atmospheric CVD syntheses. This was first demonstrated in TEM studies in which catalyst nanoparticle formation occurred only upon introduction of acetylene gas [21,23]. These observations imply that acetylene is a significantly more effective reducer of oxidized iron films at low pressure. Further, trace amounts of sputtered carbon were found to play a similar role in the reduction of film catalysts [36,37]. Because the minimum operating pressure of the Quanta ESEM (10 Pa) exceeds the partial pressure of hydrogen in previous TEM experiments (40 mT, or 0.53 Pa) by an order of magnitude, a catalyst reduction experiment was performed to observe its effectiveness as a reducing agent during in-situ SEM experiments.

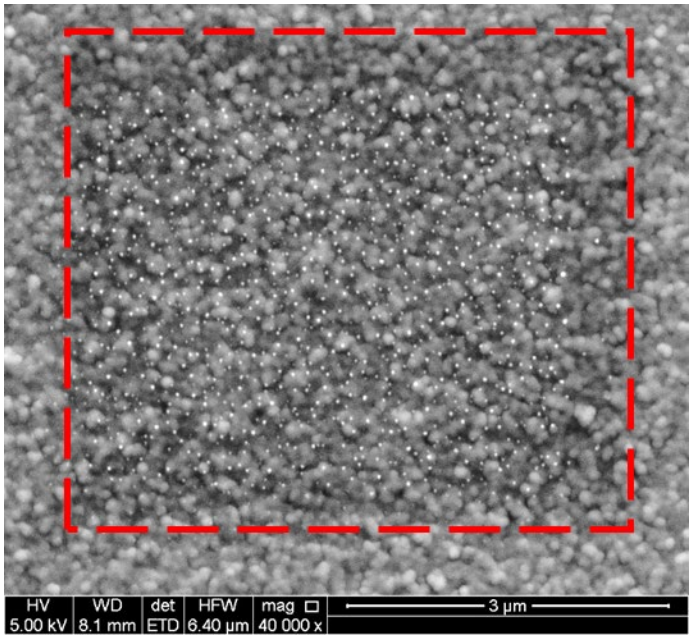

FIGURE 4. IN-SITU SEM CATALYST REDUCTION IN HIGH VACUUM. CATALYST NANOPARTICLES FORMED ONLY WITHIN THE REGION IN WHICH ADVENTITIOUS CARBON WAS DEPOSITED PRIOR TO HEATING, AS DENOTED BY THE DASHED BOX.

The catalyst reduction experiment was performed using liquid nitrogen in the cold trap to remove water vapor from the SEM environment. The chamber pressure was stabilized at 100 Pa of hydrogen prior to sample heating. Note that this pressure is two orders of magnitude greater than the partial pressure of hydrogen previously used in TEM experiments. The chip was heated to a temperature of 650ºC. The sample dwelled at the elevated temperature for 1 hour, with no observed change in the catalyst film suggesting that hydrogen alone was ineffective at reducing the iron catalyst film, as required for CNT forest synthesis. Imaging at high vacuum after the chip had cooled to room temperature confirmed that no visible catalyst nanoparticle had formed during the attempted reduction. Representative SEM images from this experiment are presented in **FIGURE 3**. Note that the background texture represents the texture of the silicon carbide heater substrate. A lack of catalyst nanoparticle formation indicates that hydrogen was insufficient at reducing the catalyst film.

In a separate catalyst evolution experiment, the role of unintentional adventitious carbon in reducing the iron catalyst was examined. In this experiment, the electron beam scanned a 5 x 5 µm area within the central heated zone of the E-chip in high vacuum mode prior to heating. The dark area enclosed within the dashed square in **FIGURE 4** represents the area of this scan and is evidence of carbon deposition. The chip was then heated to 500ºC under high-vacuum with open-loop temperature control calibrated to heat under high-vacuum conditions. Catalyst particles within the carbon deposition zone formed during the heating phase, prior to reaching the setpoint temperature. Particle formation was not observed outside of the carbon deposition area except for some small particle formation within 1 µm of the left boundary. This observation is consistent with the findings of others that trace carbon deposition enhances the reduction of iron catalyst films and the formation of catalyst nanoparticles. Note that no CNT formation was observed during this experiment.

The catalyst evolution was also evaluated at a low-pressure acetylene background, consistent with the processing conditions used for CNT forest synthesis. Based on initial experiments, the catalyst evolution behavior was inconsistent between synthesis runs, even when using seemingly identical conditions. As discussed below, catalyst nanoparticles would sometimes form and then rapidly support the growth of CNTs within seconds, consistent with in-situ TEM synthesis observations [21]. In other experiments, catalyst particle formation and CNT synthesis was supported only within regions where adventitious carbon was deposited prior to synthesis. In another subset of experiments, no CNTs were synthesized, but catalyst nanoparticles were formed within localized regions of adventitious carbon deposition. In experiments that did not support CNT forest synthesis, an extended observation of catalyst particle evolution was possible. An extended image analysis of one such experiment follows below.

3.2 Image Analysis

An in-house image processing software was used for the detection of catalyst particles and quantitative analysis of their spatial layout and evolution in time. Considering low signal-to-noise (SNR) characteristics of electron microscopy images, we have developed a multi-cue system for robust detection of catalyst particles. Beside raw image grayscale intensities, this analysis software relied on motion and change cues computed

using a tensor-based method. The proposed processing pipeline consisted of four main modules: (1) motion and change computation; (2) catalyst particle detection; (3) spatial layout description and quantification; and (4) catalyst growth analysis in time. These modules are further described below.

Structure tensors are a matrix representation of partial derivative information in an image. Since they allow both orientation estimation and image structure analysis, they have been used in many image processing and computer vision applications. 3D structure tensors have been used for motion estimation and segmentation [38]. The flux tensor [39,40] is an extension to 3D structure tensor, developed to detect only the moving or changing structures in an image sequence without expensive eigenvalue decomposition as with the 3D structure tensors. The 3D flux tensor (J_F) corresponds to the temporal variations of the optical flow field within the local 3D spatiotemporal volume. The flux tensor was computed for each position I(x,y,fr) of each frame *F* in the image sequence using a sliding window of K frames. The trace of the flux tensor (Eq. 1) was used as an indication for motion or change in an image location, where *I* refers to original SEM image intensity.

$$\mathrm{trace}(\mathrm{J_F}) = \int_{\Omega(\mathrm{x,y})} \left\| \frac{\partial}{\partial t} \nabla \mathrm{I} \right\|^2 dxdy \qquad (1)$$

Growing catalyst particles were identified as regions of high temporal change in the image. For robust identification of changing regions, frame-level motion and change levels that were indicated by the flux tensor trace were accumulated in time to compute a persistent change indicator map, *P*, for the image sequence.

$$P(x,y) = \sum_{t=0}^{N} \mathrm{trace}(\mathrm{J_F}(\mathrm{x,y,t})) \qquad (2)$$

Regional maxima of persistent change were marked as growing catalyst regions. Regional maxima are connected components of pixels with a constant intensity value, and whose external boundary pixels all have a lower value. To suppress spurious regional maxima, H-maxima transform [41] was applied to P prior to regional maxima computation. The process resulted in a binary growing catalyst versus background mask M.

$$M(x,y) = \begin{cases} 1, & P(x,y) \in \mathit{regional\ maxima} \\ 0, & \mathit{otherwise} \end{cases} \qquad (3)$$

Delaunay triangulation was applied to the centroids of the detected catalyst particles, and a catalyst neighborhood graph was generated [42–44] (see **FIGURE 5**). In this neighborhood graph, nodes corresponded to the location of a catalyst particle and edges linked immediate neighbors. For each node in this neighborhood graph, two specific neighbors, nearest immediate neighbor and farthest immediate neighbor were identified. The neighborhood graph allowed spatial point pattern analysis [45] to describe spatial layout characteristics of the catalysts. In future work, the plan is to analyze relationships between catalyst spatial layout characteristics and material properties of resulting CNT forests.

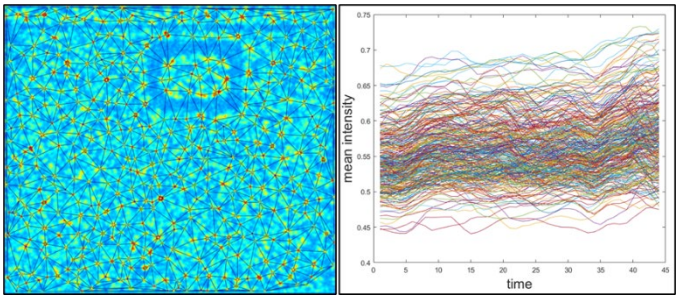

FIGURE 5. CATALYST NEIGHBORHOOD GRAPH (LEFT); CATALYST MEAN INTENSITY CHANGE IN TIME AS A MEASURE OF CATALYST GROWTH (RIGHT).

Connected component labeling was applied to the catalyst mask, M, and unique labels were assigned to each detected catalyst. These labeled masks were then projected to individual frames of the image sequence. For each uniquely labeled region of each frame in the sequence, mean SEM image intensity was computed. Considering that darker regions in the SEM image sequence correspond to background and brighter regions correspond to accumulating catalysts, the regional mean intensity was used as a proxy for catalyst size. In other words, the diameter of a catalyst particle exhibiting a larger grayscale intensity is considered to be greater than another particle having a lower grayscale intensity. **FIGURE 5** shows the catalyst neighborhood graph and catalyst mean intensity change in time for a sample catalyst evolution sequence. The intensity of the particles grows with time, indicative of nanoparticle coarsening, as observed in in-situ TEM syntheses and analysis [46]. The robustness of the technique will grow as additional catalyst evolution sequences are analyzed. Also note that the embedded blue horizontal line and rectangular outline represent boundaries of areas previously scanned by SEM, further emphasizing the role of carbon.

3.3 CNT Forest Synthesis

Ideally, CNT forest synthesis would occur across the entire heated zone of an E-chip. To date, this behavior has not yet been observed. Instead, successful syntheses have been observed in two different configurations. In one scenario, dense CNT synthesis is observed within an area of adventitious carbon deposition. When this growth mode is activated, CNT synthesis initiates at approximately 650ºC, and the resulting CNT forests may reach several hundred microns in length. A representative image sequence of catalyst particle evolution and subsequent CNT forest synthesis can be seen in **FIGURE 6**. In this image sequence, images were obtained at a rate of 20 frames / minute. The times referenced in the figure correspond to the initial frame in which catalyst particle formation occurs. Catalyst particles grow in number and diameter with time until the rapid onset of CNT forest synthesis. In this sequence, the initial image frame representing the nucleation of CNTs was not recorded because

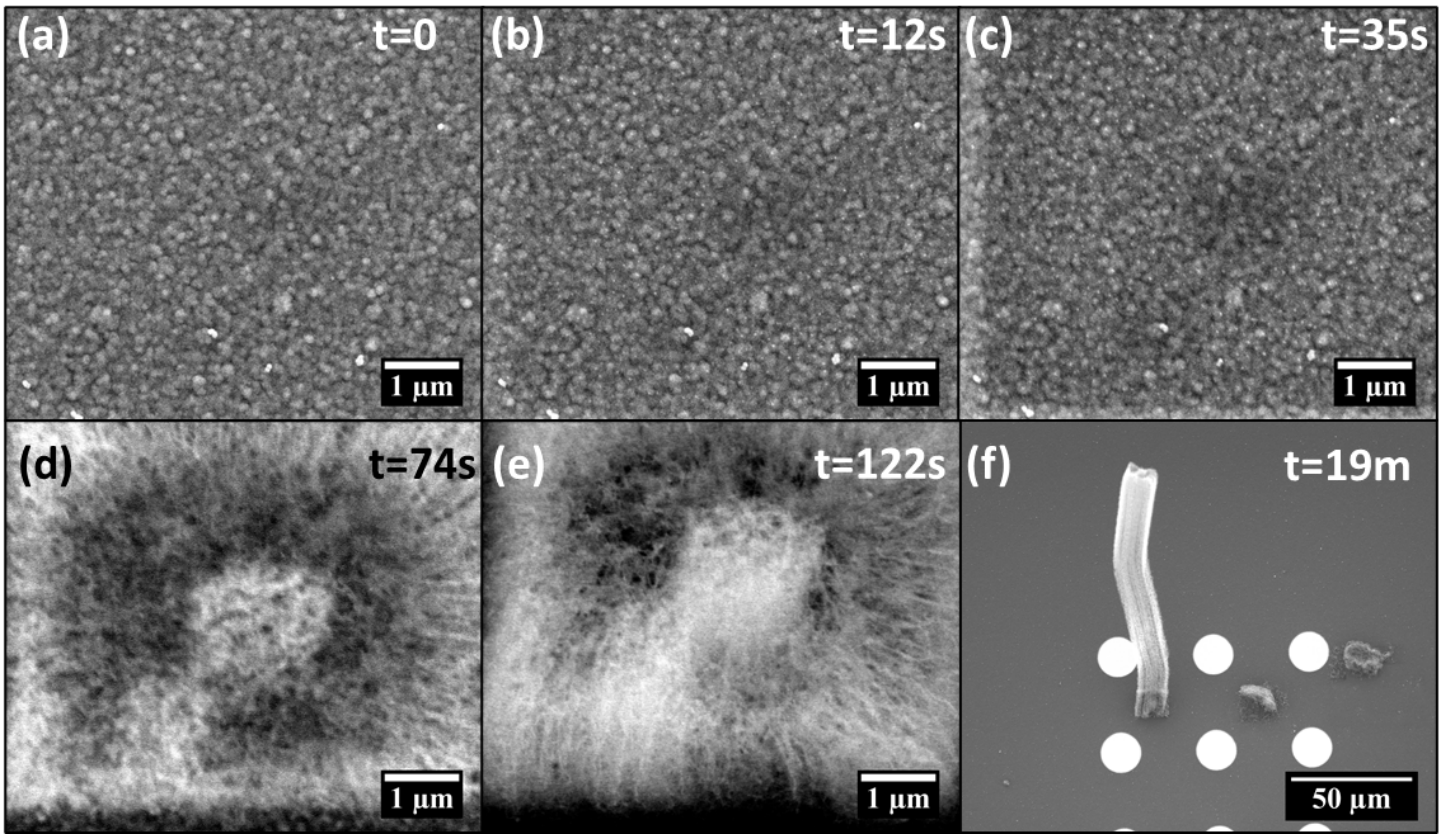

FIGURE 6. IN SITU SEM SYNTHESIS OF CNT FOREST MICROPILLAR ON A PREDEFINED PATCH OF ADVENTITIOUS CARBON DEFINED BY THE INITIAL SCAN AREA OF (A). THE SEQUENCE (A-C) SHOWS THE INITIAL CATALYST DEWETTING AND CATALYST EVOLUTION. THE SEQUENCE (D,E) SHOWS GROWTH OF A CNT FOREST WITHIN THE REGION OF ADVENTITOUS CARBON. IMAGE (F) SHOWS THE ISOLATED CNT FOREST MICROPILLAR AFTER SYNTHESIS OBTAINED AT AN ANGLE OF 45^{O}. ALL TIMES REFERENCED IN THE IMAGES ARE WITH RESPECT TO THE FIRST CATALYST PARTICLE FORMATION IN (A).

image acquisition was paused for focus adjustment. The CNT forest retains its initial cross-sectional area as it grows to a height exceeding 100 µm. Similar growth was observed for areas as large as 50 x 50 µm. Smaller regions of carbon deposition nested within larger areas of carbon deposition appear to exhibit even greater CNT growth rates than surrounding areas. An example of nested carbon deposition can be seen in **FIGURE 7**. Here, the largest green box represents one carbon deposition, the embedded black box represents a second deposition, and the small red box represents a third deposition nested within the second box. Note that accelerated CNT growth also occurred around the perimeter of the SiC holes. We stress that although the adventitious carbon promotes CNT forest synthesis, the lack of deposition control makes it non-ideal for controlled experiments.

In a second synthesis modality, CNT forest synthesis occurred well outside of the uniformly heated zone (approximately defined by the 3 x 3 array of holes). In these syntheses, the temperature of the uniformly heated zone was increased between 800-900^{o}C at 50 Pa of acetylene. At these aggressive temperatures, uniform and dense CNT forests formed as a concentric ring. A representative SEM image of such a synthesis is shown in **FIGURE 8**, accompanied by a magnified

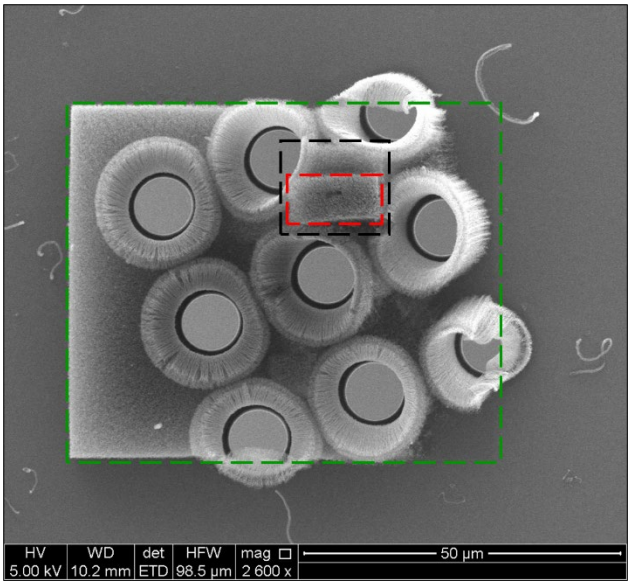

FIGURE 7. POST-SYNTHESIS TOP-DOWN SEM IMAGE OF CNT FOREST GROWTH FROM NESTED AREAS OF CARBON DEPOSITION.

view of the CNT forest morphology. It important to note that although the temperature of the uniformly heated zone was known and controlled, the temperature around the perimeter at which synthesis occurred is not known precisely. We hypothesize that the gas flow established by natural convection may produce a stagnation point in the heated region that diminishes gas flow from reaching the catalyst residing on the surface of the region of highest temperature. Catalyst migration may also contribute to this effect. Efforts are currently underway to identify the root cause of this growth mechanism and promote repeatable, uniform CNT forest synthesis.

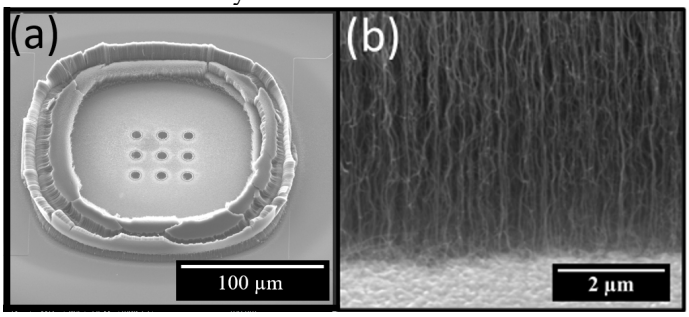

FIGURE 8. POST-SYNTHESIS SEM IMAGES OF (A) CNT FOREST SYNTHESIS AROUND THE PERIMETER OF E-CHIP HEATING ZONE AND (B) A MAGNIFIED VIEW OF THE CNT FOREST MORPHOLOGY PRODUCED BY IN-SITU SEM SYNTHESIS.

Another major challenge is balancing image resolution, noise, and temporal resolution to observe the dynamic catalyst evolution and CNT forest growth and self-assembly. For example, increasing the scan time of SEM image collection decreases the image noise at the expense of temporal resolution. Image quality may be improved by (i) using a pressure limiting aperture, (ii) decreasing the operating pressure, and (iii) reducing the image scan rate. It is desirable to collect catalyst evolution and CNT self-assembly images with enough temporal resolution and visual detail to make quantitative measurements from the data. Optimization of these parameters is ongoing.

An additional best practice to note is related to the use of a cold trap to condense water vapor and other condensable gases. Using the cold trap with liquid nitrogen enabled base pressures that are about an order of magnitude lower than that achieved without a cold finger. However, caution must be taken when using liquid nitrogen (boiling temperature -196ºC). Acetylene freezes at -82ºC at atmospheric pressure, well above the temperature of the cold finger. To avoid accumulating acetylene on the cold trap, we adopted a two-phased approach in which liquid nitrogen is initially used to rapidly reduce chamber pressure. After the chamber pressure has equilibrated, the liquid nitrogen is allowed by boil off, and dry ice (melting point -79ºC) is introduced to the cold finger to maintain SEM chamber pressure while preventing acetylene accumulation.

3.4 Perspective

The in-situ SEM synthesis of CNT forests is part of a larger strategy to map the process-structure-property relationships governing CNT forests. In-situ SEM experiments will be used to quantify the kinetics and mechanisms of CNT forest growth and self-assembly. In turn, these fundamental mechanisms will be input into a finite element mechanical numerical model that simulates the synthesis and characterization of CNT forests [47–51]. The validated simulations may then be used as a low-cost and high-throughput virtual laboratory to generate large data sets which are analogous to data obtained by physical experiments, including in-situ SEM synthesis. These data may be used to train machine learning algorithms to more widely explore the possible multi-variate parameter space available for CNT forest synthesis. As the cooperative numerical and physical experiments mature, machine learning can be used to quickly pinpoint synthesis parameters required to synthesize CNT forests with user-defined properties. Because of the vastness of the solution space, a learning algorithm will be designed to predict best physical parameter configurations.

The learning solution will fetch critical information about the state of the experimental knowledge to infer improved parameters and control the future trajectory of experiments. We envision using reinforcement learning (RL) techniques as learning agents to learn the policies and protocols of CNT growth, while having final CNT forest physical properties as a target objective function. A well-trained RL model can learn complete experimental protocols and can work in synergy with automation tools to automate CNT growth experiments to achieve desirable CNT physical properties. Thus, this approach eventually minimalizes and even removes humans from the loop and eliminates human error in judgement of the experiments. An initial catalog of setups with different synthesis parameters (temperature, pressure, gas composition, catalyst thickness, etc.) will be created after sufficient data has been collected. The catalog will be updated as additional experiments are performed, while a RL model will learn correlations between the input synthesis parameters and the resultant CNT forest morphology and physical properties (measured externally). Through this approach, we will generate multiple RL models which can act as custom templates for different desired results of the experiments while gradually removing the need for having a human in the loop to determine experimental conditions and conduct the prescribed experiments.

4. CONCLUSION

We have demonstrated the use of environmental SEM as a viable tool to support in-situ CVD synthesis of CNT forests. While the in-situ TEM synthesis of CNT forests has been demonstrated previously, use of SEM presents unique challenges and considerations that must be taken into account to acquire relevant data. This work details initial efforts to establish best practices for the synthesis procedure and some initial synthesis results. We believe that the protocols detailed within this work may be used by others to accelerate the optimization of synthesis parameters for similar in-situ SEM synthesis studies.

Initial in-situ synthesis results indicate that SEM has sufficient spatial resolution to capture the formation and evolution of catalyst nanoparticles and individual growing

CNTs. Further, we demonstrate that the unintended deposition of adventitious carbon enhances the formation of catalyst nanoparticles and subsequent CNTs and may potentially be used to pattern cross section of CNT forest micropillars in the future. We also observe uniform CNT forest synthesis occurring only in areas that are distant from the central heating zone. Though further optimization is required, this study presents strong proof-of-concept results towards uniform in-situ SEM CNT forest synthesis.

In future experiments, we plan to validate CNT forest numerical simulations using observations obtained with in-situ SEM synthesis. By integrating simulation and physical experiments, we will train machine learning algorithms that can help identify the processing parameters required to fabricate CNT forests with user-specified properties.

ACKNOWLEDGEMENTS

The authors would like to acknowledge funding from National Science Foundation (NSF) under award CCMI 2026847 and CMMI 1651538 (authors GK and MRM), and partial support from NSF MRI CNS-1429294 and Army Research Laboratory award W911NF-1820285 (for KP, RB and FB).

REFERENCES

[1] Garcia, E. J., Wardle, B. L., John Hart, A., and Yamamoto, N., 2008, "Fabrication and Multifunctional Properties of a Hybrid Laminate with Aligned Carbon Nanotubes Grown In Situ," Compos. Sci. Technol., **68**(9), pp. 2034–2041.

[2] Wicks, S. S., de Villoria, R. G., and Wardle, B. L., 2010, "Interlaminar and Intralaminar Reinforcement of Composite Laminates with Aligned Carbon Nanotubes," Compos. Sci. Technol., **70**(1), pp. 20–28.

[3] Maschmann, M. R., Ehlert, G. J., Dickinson, B. T., Phillips, D. M., Ray, C. W., Reich, G. W., and Baur, J. W., 2014, "Bioinspired Carbon Nanotube Fuzzy Fiber Hair Sensor for Air-Flow Detection," Adv. Mater., **26**(20), pp. 3230–3234.

[4] Maschmann, M. R., Dickinson, B., Ehlert, G. J., and Baur, J. W., 2012, "Force Sensitive Carbon Nanotube Arrays for Biologically Inspired Airflow Sensing," Smart Mater. Struct., **21**(9), p. 094024.

[5] Park, M., Cola, B. A., Siegmund, T., Xu, J., Maschmann, M. R., Fisher, T. S., and Kim, H., 2006, "Effects of a Carbon Nanotube Layer on Electrical Contact Resistance between Copper Substrates," Nanotechnology, **17**(9).

[6] Franklin, A. D., Luisier, M., Han, S. J., Tulevski, G., Breslin, C. M., Gignac, L., Lundstrom, M. S., and Haensch, W., 2012, "Sub-10 Nm Carbon Nanotube Transistor," Nano Lett., **12**(2), pp. 758–762.

[7] Xu, J., and Fisher, T. S., 2006, "Enhancement of Thermal Interface Materials with Carbon Nanotube Arrays," Int. J. Heat Mass Transf., **49**(9–10), pp. 1658–1666.

[8] Cola, B. A., Xu, J., Cheng, C., Xu, X., Fisher, T. S., and Hu, H., 2007, "Photoacoustic Characterization of Carbon Nanotube Array Thermal Interfaces," J. Appl. Phys.

[9] Maschmann, M. R., Zhang, Q., Du, F., Dai, L., and Baur, J., 2011, "Length Dependent Foam-like Mechanical Response of Axially Indented Vertically Oriented Carbon Nanotube Arrays," Carbon N. Y., **49**(2).

[10] Zbib, A. A., Mesarovic, S. D., Lilleodden, E. T., McClain, D., Jiao, J., and Bahr, D. F., 2008, "The Coordinated Buckling of Carbon Nanotube Turfs under Uniform Compression," Nanotechnology, **19**(17), p. 175704.

[11] Maschmann, M. R., Zhang, Q., Wheeler, R., Du, F., Dai, L., and Baur, J., 2011, "In Situ SEM Observation of Column-like and Foam-like CNT Array Nanoindentation," ACS Appl. Mater. Interfaces, **3**(3).

[12] Brieland-Shoultz, A., Tawfick, S., Park, S. J., Bedewy, M., Maschmann, M. R., Baur, J. W., and Hart, A. J., 2014, "Scaling the Stiffness, Strength, and Toughness of Ceramic-Coated Nanotube Foams into the Structural Regime," Adv. Funct. Mater., **24**(36).

[13] Davis, B. F., Yan, X., Muralidharan, N., Oakes, L., Pint, C. L., and Maschmann, M. R., 2016, "Electrically Conductive Hierarchical Carbon Nanotube Networks with Tunable Mechanical Response," ACS Appl. Mater. Interfaces, **8**(41).

[14] Hutchens, S. B., Hall, L. J., and Greer, J. R., 2010, "In Situ Mechanical Testing Reveals Periodic Buckle Nucleation and Propagation in Carbon Nanotube Bundles," Adv. Funct. Mater., **20**(14), pp. 2338–2346.

[15] Cao, A., Dickrell, P. L., Sawyer, W. G., Ghasemi-Nejhad, M. N., and Ajayan, P. M., 2005, "Super-Compressible Foamlike Carbon Nanotube Films," Science (80-.)., **310**(5752), pp. 1307–1313.

[16] Maschmann, M. R., Ehlert, G. J., Tawfick, S., Hart, A. J., and Baur, J. W., 2014, "Continuum Analysis of Carbon Nanotube Array Buckling Enabled by Anisotropic Elastic Measurements and Modeling," Carbon N. Y., **66**, pp. 377–386.

[17] Pathak, S., Lim, E. J., Pour Shahid Saeed Abadi, P., Graham, S., Cola, B. A., and Greer, J. R., 2012, "Higher Recovery and Better Energy Dissipation at Faster Strain Rates in Carbon Nanotube Bundles: An in-Situ Study," ACS Nano.

[18] Amama, P. B., Pint, C. L., Kim, S. M., McJilton, L., Eyink, K. G., Stach, E. A., Hauge, R. H., and Maruyama, B., 2010, "Influence of Alumina Type on the Evolution and Activity of Alumina-Supported Fe Catalysts in Single-Walled Carbon Nanotube Carpet Growth," *ACS Nano*.

[19] Seung Min Kim, Cary, L. P., Placidus, B. A., Dmitri, N. Z., Robert, H. H., Maruyama, B., and Stach, E. A., 2010, "Evolution in Catalyst Morphology Leads to Carbon Nanotube Growth Termination," J. Phys. Chem. Lett.

[20] Pattinson, S. W., Diaz, R. E., Stelmashenko, N. A., Windle, A. H., Ducati, C., Stach, E. A., and Koziol, K. K. K., 2013, "In Situ Observation of the Effect of Nitrogen on Carbon Nanotube Synthesis," Chem. Mater., **25**(15), pp. 2921–2923.

[21] Balakrishnan, V., Bedewy, M., Meshot, E. R., Pattinson, S. W., Polsen, E. S., Laye, F., Zakharov, D. N., Stach, E. A., and Hart, A. J., 2016, "Real-Time Imaging of Self-Organization and Mechanical Competition in Carbon Nanotube Forest Growth," ACS Nano, **10**(12), pp. 11496–11504.

[22] Yasuda, A., Kawase, N., and Mizutani, W., 2002, "Carbon-Nanotube Formation Mechanism Based on in Situ TEM Observations," J. Phys. Chem. B, **106**(51), pp. 13294–13298.

[23] Bedewy, M., Viswanath, B., Meshot, E. R., Zakharov, D. N., Stach, E. A., and Hart, A. J., 2016, "Measurement of the Dewetting, Nucleation, and Deactivation Kinetics of Carbon Nanotube Population Growth by Environmental Transmission Electron Microscopy," Chem. Mater.

[24] Dee, N. T., Li, J., Orbaek White, A., Jacob, C., Shi, W., Kidambi, P. R., Cui, K., Zakharov, D. N., Janković, N. Z., Bedewy, M., Chazot, C. A. C., Carpena-Núñez, J., Maruyama,

B., Stach, E. A., Plata, D. L., and Hart, A. J., 2019, "Carbon-Assisted Catalyst Pretreatment Enables Straightforward Synthesis of High-Density Carbon Nanotube Forests," Carbon N. Y., **153**, pp. 196–205.

[25] Huang, X., Farra, R., Schlögl, R., and Willinger, M. G., 2019, "Growth and Termination Dynamics of Multiwalled Carbon Nanotubes at Near Ambient Pressure: An in Situ Transmission Electron Microscopy Study," Nano Lett., **19**(8), pp. 5380–5387.

[26] Bedewy, M., and Hart, A. J., 2013, "Mechanical Coupling Limits the Density and Quality of Self-Organized Carbon Nanotube Growth," Nanoscale.

[27] Bedewy, M., Meshot, E. R., Reinker, M. J., and Hart, A. J., 2011, "Population Growth Dynamics of Carbon Nanotubes," ACS Nano.

[28] Meshot, E. R., Verploegen, E., Bedewy, M., Tawfick, S., Woll, A. R., Green, K. S., Hromalik, M., Koerner, L. J., Philipp, H. T., Tate, M. W., Gruner, S. M., and Hart, A. J., 2012, "High-Speed in Situ X-Ray Scattering of Carbon Nanotube Film Nucleation and Self-Organization," ACS Nano.

[29] Nikolaev, P., Hooper, D., Webber, F., Rao, R., Decker, K., Krein, M., Poleski, J., Barto, R., and Maruyama, B., 2016, "Autonomy in Materials Research: A Case Study in Carbon Nanotube Growth," npj Comput. Mater., **2**(1), p. 16031.

[30] Nikolaev, P., Hooper, D., Perea-López, N., Terrones, M., and Maruyama, B., 2014, "Discovery of Wall-Selective Carbon Nanotube Growth Conditions via Automated Experimentation," ACS Nano.

[31] "Fusion Brochure" [Online]. Available: http://protochips.com/wp-content/uploads/2017/10/Fusion-Brochure.pdf.

[32] Rao, R., Carpena-Núñez, J., Dee, N. T., Zakharov, D. N., Boscoboinik, J. A., Stach, E. A., Hart, A. J., and Maruyama, B., 2020, "Maximization of Carbon Nanotube Yield by Solid Carbon-Assisted Dewetting of Iron Catalyst Films," Carbon N. Y., **165**, pp. 251–258.

[33] Carpena-Núñez, J., Boscoboinik, J. A. J. A., Saber, S., Rao, R., Zhong, J.-Q. J. Q., Maschmann, M. R. M. R., Kidambi, P. R., Dee, N. T. N. T., Zakharov, D. N. D. N., Hart, A. J. J., Stach, E. A. E. A., and Maruyama, B., 2019, "Isolating the Roles of Hydrogen Exposure and Trace Carbon Contamination on the Formation of Active Catalyst Populations for Carbon Nanotube Growth," ACS Nano, **13**(8), pp. 8736–8748.

[34] Nath, S. K., and Palaniappan, K., 2005, "Adaptive Robust Structure Tensors for Orientation Estimation and Image Segmentation," *Lecture Notes in Computer Science (Including Subseries Lecture Notes in Artificial Intelligence and Lecture Notes in Bioinformatics)*, Springer, Berlin, Heidelberg, pp. 445–453.

[35] Bunyak, F., Palaniappan, K., Nath, S. K., and Seetharaman, G., 2007, "Geodesic Active Contour Based Fusion of Visible and Infrared Video for Persistent Object Tracking," *Proceedings - IEEE Workshop on Applications of Computer Vision, WACV 2007*, IEEE Computer Society.

[36] Bunyak, F., Palaniappan, K., Nath, S. K., and Seetharaman, G., 2007, "Flux Tensor Constrained Geodesic Active Contours with Sensor Fusion for Persistent Object Tracking," J. Multimed., **2**(4), pp. 20–33.

[37] Soille, P., 2013, *Morphological Image Analysis: Principles and Applications*, Springer Science \& Business Media.

[38] Nath, S. K., Palaniappan, K., and Bunyak, F., 2006, "Cell Segmentation Using Coupled Level Sets and Graph-Vertex Coloring.," Med. Image Comput. Comput. Assist. Interv., **9**(Pt 1), pp. 101–108.

[39] Ersoy, I., Bunyak, F., Higgins, J. M., and Palaniappan, K., 2012, "Coupled Edge Profile Active Contours for Red Blood Cell Flow Analysis," *Proceedings - International Symposium on Biomedical Imaging*, pp. 748–751.

[40] Gronkiewicz, K. M., Giuliano, E. A., Kuroki, K., Bunyak, F., Sharma, A., Teixeira, L. B. C., Hamm, C. W., and Mohan, R. R., 2016, "Development of a Novel in Vivo Corneal Fibrosis Model in the Dog," Exp. Eye Res.

[41] Baddeley, A., Rubak, E., and Turner, R., 2015, *Spatial Point Patterns: Methodology and Applications with R*, CRC press.

[42] Ezzat, A. A., and Bedewy, M., 2020, "Machine Learning for Revealing Spatial Dependence among Nanoparticles: Understanding Catalyst Film Dewetting via Gibbs Point Process Models," J. Phys. Chem. C, **124**(50), pp. 27479–27494.

[43] Maschmann, M. R., 2015, "Integrated Simulation of Active Carbon Nanotube Forest Growth and Mechanical Compression," Carbon N. Y., **86**, pp. 26–37.

[44] Brown, J., Hajilounezhad, T., Dee, N. T. N. T., Kim, S., Hart, A. J. J., and Maschmann, M. R. M. R., 2019, "Delamination Mechanics of Carbon Nanotube Micropillars," ACS Appl. Mater. Interfaces, **11**(38), pp. 35221–35227.

[45] Taher Hajilounezhad, Rina Bao, Kannappan Palaniappan, Filiz Bunyak, Prasad Calyam, M. R. M., "Discovering Carbon Nanotube Forest Process-Structure-Property Relationships Using High-Throughput Simula-Tion and Deep Learning."

[46] T. Hajilounezhad, R. Surya, Z. Oraibi, F. Bunyak, K. Palaniappan, P. Calyam, M. R. M., 2019, "Rapid Exploration of Carbon Nanotube Forest Synthesis-Structure-Property Relationships Using Physics-Based Simulation and Deep Learning," *ASME IMECE*, Salt Lake City, UT.

[47] Taher Hajilounezhad, Rina Bao, Kannappan Palaniappan, Filiz Bunyak, Prasad Calyam, M. R. M., "Predicting Carbon Nanotube Forest Synthesis Attributes and Mechanical Properties Using High-Throughput Simulation and Deep Learning," npj Comput. Mater.